Journal of Alloys and Compounds 872 (2021) 159608

Contents lists available at ScienceDirect

Journal of Alloys and Compounds

journal homepage: www.elsevier.com/locate/jalcom

Three-dimensional nano/micro-structured porous MoP/CNTs microspheres as high-capacity anode for lithium-ion batteries

Yangbo Wang[a,1], Deyang Zhang[a,c,*,1], Ya Yang[a], Ying Guo[a], Zuxue Bai[a], Paul K. Chu[c], Yongsong Luo[a,b,*]

[a] Key Laboratory of Microelectronics and Energy of Henan Province, Henan Joint International Research Laboratory of New Energy Storage Technology, Xinyang Normal University, Xinyang d6d000, PR China
[b] College of Physics and Electronic Engineering, Nanyang Normal University, Nanyang 473061, PR China
[c] Department of Physics, Department of Materials Science & Engineering, and Department of Biomedical Engineering, City University of Hong Kong, Tat Chee Avenue, Kowloon, Hong Kong, China

ARTICLE INFO

Article history:
Received 23 December 2020
Received in revised form 25 February 2021
Accepted 19 March 2021
Available online 24 March 2021

Keywords:
Lithium ion batteries
Molybdenum phosphide
Carbon nanotubes
Nano/micro-structured materials

ABSTRACT

Molybdenum phosphide (MoP) is considered one of the promising electro-active materials for lithium-ion batteries (LIBs) owing to the high theoretical capacity but development of MoP anodes faces challenges such as the poor cycle stability. Herein, we propose a facile strategy to synthesize MoP/CNTs microspheres from a spray drying method followed by a phosphating process. The carbon nanotubes (CNTs) are inlaid throughout the MoP/CNTs microspheres, which not only promotes the electrical conductivity of the composite, but also relieves volume change during cycling. Benefit from the synergistic effect by coupling the MoP nanoparticles with CNTs and the nano/micro structure, the anode material of porous MoP/CNTs microspheres shows excellent cycling stability and specific capacity, for example, a capacity of 1568 mAh g^{-1} for 300 cycles at 200 mA g^{-1}. Quantitative kinetics analysis reveals that the charge storage mechanism of MoP/CNTs mainly relies on pseudocapacitance behavior, especially at high scan rates (86.6% at 0.5 mV s^{-1}), which improves the lithium storage performance at high scan rates. Our results provide insights into the design and synthesis of the functional materials with nano-micro structure for high-performance LIBs.

1. Introduction

Lithium-ion batteries (LIBs) are very common nowadays in electric vehicles due to the long cycling life, high energy density, minimal memory effects, good durability, as well as environmental benignity [1–4]. Nevertheless, owing to the increasing demand for higher specific capacity and energy density, graphite anodes with low specific capacity (372 mAh g^{-1}) need improvement or replacement [5,6]. Therefore, development of new advanced anode materials with high energy density, long cycling life, and rate performance to replace the traditional anode material is necessary, albeit challenging.

A variety of anode materials such as transition metal oxides, sulfides and phosphates [7,8] has been studied and in particular, transition metal phosphides are quite attractive owing to the high theoretical capacity, small electrode polarization, and small potential range (0.5–1 V) in the lithiation/delithiation potential [9–11]. Such small potential range avoids the deposition potential of Li^+ and averts the growth of lithium dendrites [10]. In addition, Li_3P produced during charging and discharging of transition metal phosphides has higher ion conductivity (~10^{-4} S cm^{-1}) than lithium conductors in conventional LIBs anode materials such as Li_2O in metal oxide (~5×10^{-8} S cm^{-1}) and Li_2S in metal sulfide (~10^{-13} S cm^{-1}) [12,13]. Moreover, the anode materials with the conversion reaction can show high specific capacity [14,15]. Therefore, much attention has been paid to phosphorus-based materials such as CoP [16], Cu_3P [17], NiP_2 [18], MoP [19], Sn_3P_4 [20], and Fe_2P [21], and apply them to anode materials for LIBs.

MoP has a high theoretical capacity (632 mAh g^{-1}), moderate operation potential, and good electrochemical activity, which is very promising anode materials for LIBs among the phosphorus-based

* Corresponding authors at: Key Laboratory of Microelectronics and Energy of Henan Province, Henan Joint International Research Laboratory of New Energy Storage Technology, Xinyang Normal University, Xinyang d6d000, PR China.
E-mail addresses: zdy@xynu.edu.cn (D. Zhang), ysluo@xynu.edu.cn (Y. Luo).
[1] These authors contributed equally to this work.

https://doi.org/10.1016/j.jallcom.2021.159608
0925-8388/

materials [22–24]. One major advantage of MoP electrode is that charge storage is based on the conversion reaction, so they have larger energy densities than conventional electrode materials based on the intercalation mechanism in charge storage [25]. However, MoP suffers from drawbacks such as the low electrical conductivity, large volume change, and sluggish ion transport, which tend to be common in materials with based on the conversion reaction. Resulting pulverization and exfoliation of electrode materials can cause electrical contact loss, fast capacity fading, and poor rate capability [14]. Cho et al. [26] reported that the MoP_2 synthesized by a mechanochemical method had only a capacity of 500 mAh g^{-1} after 60 cycles at 200 mA g^{-1}. Chai et al. [27] implemented a two-step route to prepare MoP-C microspheres via carbonization and phosphorization to produce anode materials for LIBs but the MoP-C microspheres only showed poor cycling performance of 1152 mAh g^{-1} after 150 cycles at 200 mA g^{-1}. Liu et al. [28] fabricated MoP@nitrogen-doped carbon nanofibers by electrostatic spinning but the capacity of the MoP@NCNFs electrode was only 300 mAh g^{-1} after 500 cycles at 200 mAh g^{-1}. Therefore, a lot of effort is needed to improve the electrochemical performances of molybdenum phosphide as anode materials in LIBs. Molybdenum phosphide has been combined with carbonaceous materials such as carbon nanotubes (CNTs) to improve its lithium storage property [29]. It is well known that CNTs have high mechanical strength and an intrinsic conductivity of 10^4 S cm^{-1} due to the micron-scale length and sp^2 lattice [30,31]. Based on that, introduction of CNTs could significantly improve the electrical conductivity and structure stability of the composites, resulting in improved performances as the anode materials in LIBs. Based on the volume expansion of active materials during cycling, we designed and synthesized MoP/CNTs microspheres with the synergistic effect of microsphere and inlaid structure, and MoP/CNTs microspheres with larger specific surface area also have more active sites.

Herein, a facile and safe strategy to fabricate MoP/CNTs by spray drying in conjunction with a phosphating process is designed and described. The CNTs are inlaid throughout the microspheres to provide not only a 3D conductive network for fast charging and ion transport, but also adequate space to alleviate volume change during cycling. In addition, the CNTs avoid aggregation of the MoP nanoparticles. The LIB anode composed of MoP/CNTs shows outstanding cycling performance and stability at 200 mA g^{-1} after 300 cycles with a high capacity of 1568 mAh g^{-1}. As the current rate is increased, the contribution of pseudocapacitance increases leading to excellent electrochemical performance of MoP/CNTs microspheres as anode materials in LIBs.

2. Results and discussion

The schematic diagram of the preparation of the MoP/CNTs microspheres is depicted in Fig. 1. The samples obtained by spray drying were annealed and phosphated to obtain Mo_2C/CNTs and MoP/CNTs in turn, and NaH_2PO_2 is the key agent in the phosphating process. NaH_2PO_2 decomposes upon heating to disproportionally generate PH_3 which works as the phosphating agent. The Mo_2C/CNTs and MoP/CNTs samples all maintain the morphology of microspheres. The final MoP/CNTs microspheres was based on CNT as 3D skeleton, in which MoP nanoparticles were embedded on the surface of CNT.

The scanning electron microscopy images (SEM) of the Mo_2C/CNTs microspheres in Fig. S1 show that the Mo_2C/CNTs sample with a diameter of 1–2 μm has a microsphere morphology. The CNT/Mo salt/sucrose sample is annealed at 800 °C in Ar atmosphere to obtain the intermediate product Mo_2C/CNTs with the microsphere morphology (Fig. S1a–c). After phosphating, MoP/CNTs keeps the microsphere structure as depicted in Fig. 2a–c. As shown in Fig. 2a, the size of the MoP/CNTs microspheres is still 0.5–2 μm, which is inherited from the Mo_2C/CNTs microspheres. We observed the curved CNTs on the surface of MoP/CNTs microspheres (Fig. 2b, c and Fig. S2a, b), which further proves the existence of 3D CNTs skeleton in microspheres. This structure not only shortens the diffusion paths of ions and electrons, but also alleviates volume change during lithiation/delithiation process [32]. Two MoP/CNTs microspheres with the same size (1.5 μm) are clearly shown in Fig. 2d. As can be seen from the transmission electron microscope (TEM) images (Fig. S3) of Mo_2C/CNTs microspheres, the diameter of the microsphere is 0.5–2 μm , which further proves that MoP/CNTs microspheres inherits the diameter of Mo_2C/CNTs microspheres. The TEM image (Fig. 2e) discloses the porous microspheres structure of MoP/CNTs. More importantly, the MoP nanoparticles are embedded in the CNTs as shown by the larger image in the red box in Fig. 2e. This microspheres-like structure has a large Brunauer-Emmett-Teller (BET) specific surface area of 113.4 m^2 g^{-1} as obtained by the N_2 adsorption/desorption isotherms (Fig. S3a). The pore size distribution acquired by Barrett-Joyner-Halenda method analysis reveals that MoP/CNTs contain massive mesopores, which can provide abundant ion diffusion channels (Fig. S3b) [33]. In fact, the value of MoP/CNTs is larger than that of the Mo_2C/CNTs microspheres (17.5 m^2 g^{-1}). Compared to Mo_2C/CNTs (Fig. S3c and d), MoP/CNTs possesses a larger specific surface area arising from the release and penetration PH_3 gas produced by sodium hypophosphate as well as dehydration [34–37]. The large surface area leads to more contact with lithium ions of electrolyte, so as to improve the storage performance of lithium [38]. The high resolution TEM image (HRTEM) of MoP/CNTs in Fig. 2f shows lattice fringes with an inter-planar spacing (d) of 0.21 nm corresponding to the (101) plane of hexagonal MoP (PDF#65-6487). The low-magnification SEM image are shown in Fig. 2g and the corresponding energy dispersive X ray spectrometer (EDX) maps acquired from MoP/CNTs microspheres. Mo, P, and C elements are evenly distributed in the microspheres as showed in Fig. 2h–j.

The X-ray diffraction (XRD) pattern of Mo_2C/CNTs sample are presented in Fig. S2. The diffraction peaks at 34.4°, 38.0°, 39.4°, 52.1°, 61.5°, 69.7°, 72.4° 74.6° and 75.5° from Mo_2C/CNTs microspheres correspond to the (100), (002), (101), (102), (110), (103), (200), (112) and (201) plane of monoclinic Mo_2C (PDF#35-0787). There is also a weak carbon peak at 26°. The XRD pattern of MoP/CNTs in Fig. 3a confirms the hexagonal MoP phase and it is in line with previous observation [39]. The diffraction peaks at 28.0°, 32.0°, 43.0°, 57.1°, 57.7°, 64.8°, 67.0° 67.6° and 74.1° stem from the (001), (100), (101), (110), (002), (111), (200), (102) and (201) plane of monoclinic MoP (PDF#65-6487), whose crystal structure is shown in Fig. 3b. Thermogravimetric (TG) curves of MoP/CNTs and Mo_2C/CNTs are shown in Fig. S4, and the final product of them is MoO_2 after a specific program of heating in air. According to the principle of Mo quality constant, we calculated the contents of MoP and Mo_2C in MoP/CNTs and Mo_2C/CNTs samples were 85.2% and 68.5%, respectively.

To study the valence states of MoP/CNTs, X-ray photoelectron spectroscopy (XPS) is performed and the results are shown in Fig. 3c–f. The survey spectrum of MoP/CNTs (Fig. 3c) discloses Mo, P and C signals, which further demonstrated the existence of MoP and CNT in this material. In the fitted Mo 3d spectrum (Fig. 3d), the two peaks at 236.2 and 233.2 eV can be assigned to Mo $3d_{3/2}$ and $3d_{5/2}$ of MoO_3, respectively and the two peaks located at 232.4 eV and 228.8 eV are associated with Mo $3d_{3/2}$ and $3d_{5/2}$ of MoO_2. The reason for a high valence state of molybdenum is that the surfaces of MoP are partially oxidized in air. The two double peaks at 231.6 eV and 228.4 eV represent MoP species [27]. The deconvoluted peaks for the P 2p spectra at 130.6 and 129.6 eV are associated with P $2p_{1/2}$ and $2p_{3/2}$ of P-Mo bond (Fig. 3e) [40], respectively. The peaks at 133.7 eV and 134.8 eV are attributed to P–C bond and P–O bond, and P–O is derived from PO_4^{3-} and P_2O_5 formed by the oxidation of MoP surface [41–45]. The C 1s spectra (Fig. 3f) shows that peaks at 287.1, 285.3, 284.6 and 283.7 eV can be associated with C=O, C–O, C–C/C=C, and

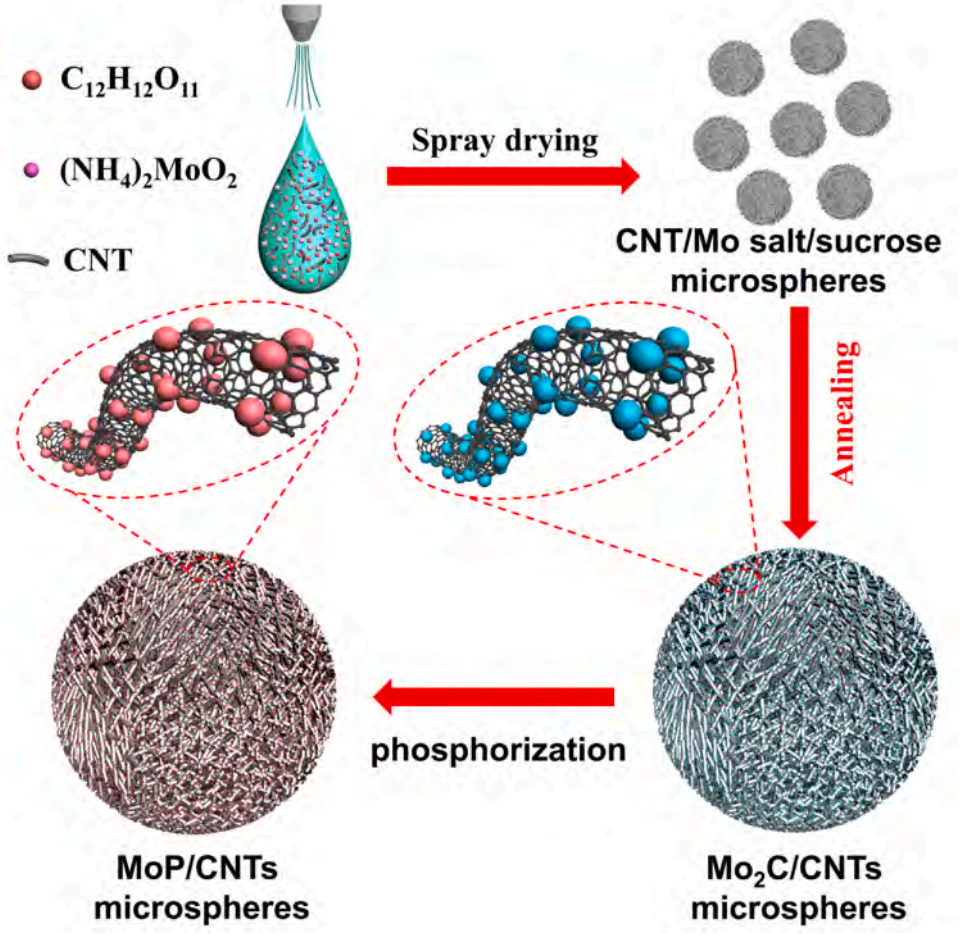

Fig. 1. Schematic illustration of the preparation of the MoP/CNTs microspheres.

C–P further confirming that the MoP particles and CNTs are chemically bound by C–P bonds [34,44,46,47].

The voltammograms (CVs) curves of the MoP/CNTs electrode with a sweep rate of 0.1 mV s^{-1} was shown in Fig. 4a. A cathodic peak appears at 0.60 V in the first cathodic sweep, which can be assigned to decomposition of electrolyte and the formation of solid electrolyte interface (SEI) film [48]. A redox pair peaks centered at 1.13/1.51 V in the subsequent cycles, is attributed to lithiation/delithiation of Li^+ [38,49]. The galvanostatic discharge/charge curves of the MoP/CNTs obtained at 200 mA g^{-1} in a range from 0.01 to 3.0 V, as shown in Fig. 4b. The initial discharge/charge capacities of MoP/CNTs are about 1860 and 1722 mAh g^{-1}, respectively and the coulombic efficiency is 92.5%. The large loss of irreversible capacity in the first cycle arises from the irreversible processes affected by the formation of SEI film [50]. For the 2nd cycle, the 2nd discharge/charge capacities of MoP/CNT were about 1702/1690 mAh g^{-1}. The coulombic efficiency at the 2nd, 5th, 10th and 300th cycle increases to 98.9%, 99.2%, 99.8%, and 99.9%, respectively, due to reversible lithium ions insertion during cycling.

The cyclabilities of MoP/CNTs and Mo_2C/CNTs are evaluated at a current density of 200 mA g^{-1} as shown in Fig. 4c. The initial discharge/charge specific capacities of MoP/CNTs are 1858/1724 mAh g^{-1} and the coulombic efficiency is 92.7%. The capacity loss is associated with irreversible processes including insertion of lithium-ion into the MoP lattice as well as formation of the SEI film [51]. Over long cycle process, the MoP/CNTs electrode still displayed pretty cycling stability with pimping capacity attenuation, for example, discharge capacity of 1568 mAh g^{-1} after 300 cycles, which is better than that of Mo_2C/CNTs (902 mAh g^{-1}). From the SEM images (Fig. S7) of the MoP/CNTs electrode after 300 cycles, it can be seen that there is almost no damage to the structure of MoP/CNTs microspheres, which further proves that MoP/CNTs has good cycling stability. This result further indicating that the performance of Mo_2C/CNTs after phosphorization (MoP/CNTs) got a big promotion. It is worth mentioning that MoP/CNTs presented pretty capabilities of 1871, 1503, 1222 and 810 mAh g^{-1} at current densities of 100, 200, 500, and 1000 mA g^{-1}, respectively (Fig. 4d). Even when the rate be set to 1000 mA g^{-1}, the capacity still reserves 810 mAh g^{-1}. When the current density is returned to 100 mA g^{-1}, a capacity of 1675 mAh g^{-1} is remained indicating outstanding rate capacity. Compared with the Mo_2C/CNTs, MoP/CNTs showed relatively high rate capabilities, indicating that it possess excellent electrochemical performance during cycling.

The long-term cycling stability at high current density is an important criterion for practical applications, which is evaluated at a rate of 1000 mA g^{-1} (Fig. 4e). MoP/CNTs exhibits 668 mAh g^{-1} after 1000 cycles along with coulombic efficiency of 99% at 1000 mA g^{-1}, which should be assigned to the lithiation-induced reactivation and stabilization of MoP [52,53]. The rapid decay of the early capacity is mainly due to the formation and instability of SEI film, especially at high current density. Due to the stabilization of SEI film and the activation of active materials, the late capacity decay is slow [11,19,28]. Better accommodation of lithium-ion improves the accessibility of lithium-ion during long-term cycling so that utilization of MoP is enhanced. Compared with other metal phosphide anode materials reported in the literature, the MoP/CNTs anode has excellent reversible capacity as shown in Table S1.

To explore the lithium storage behavior of MoP/CNTs, an analysis of the kinetics was carried out. The CV curves of the MoP/CNTs

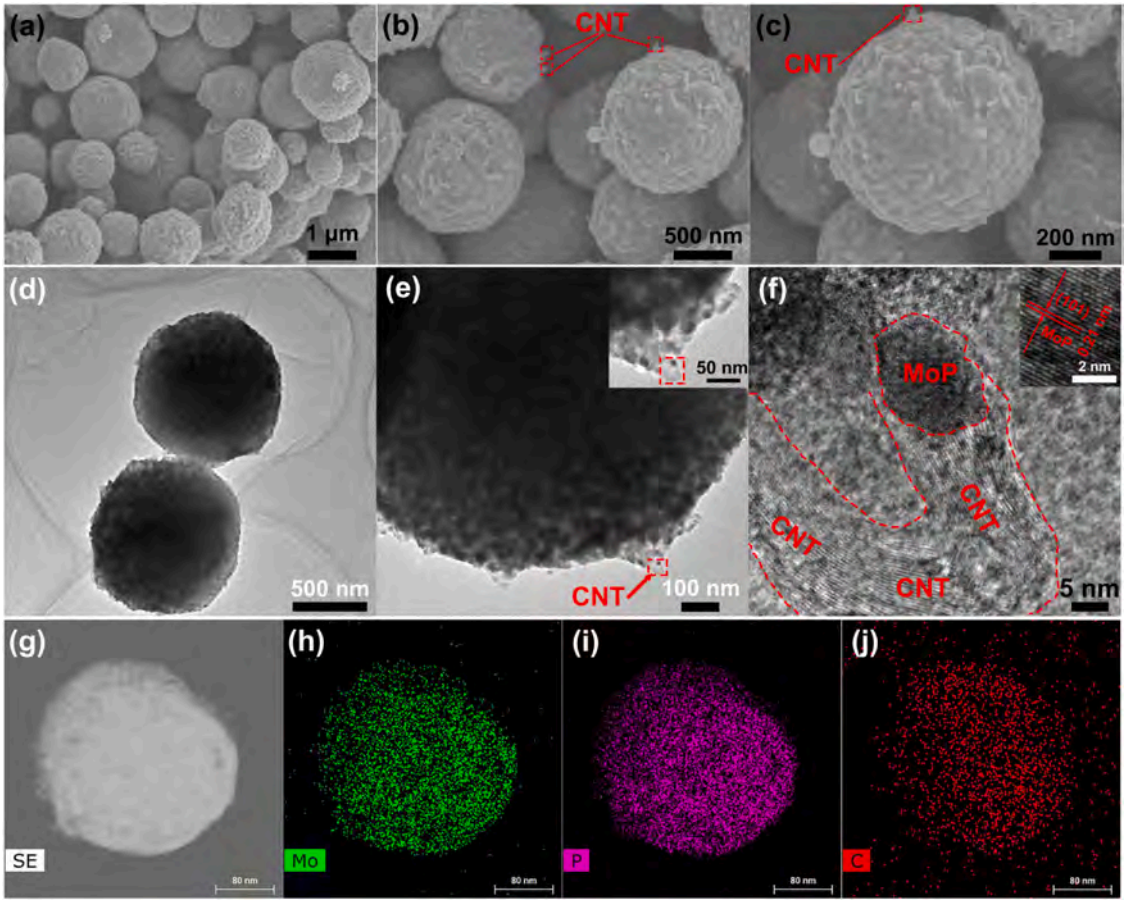

Fig. 2. (a–c) SEM images of MoP/CNTs microspheres. (d–f) TEM images of MoP/CNTs microspheres. (g–j) SEM image and the corresponding elemental mapping of Mo, P and C for MoP/CNTs.

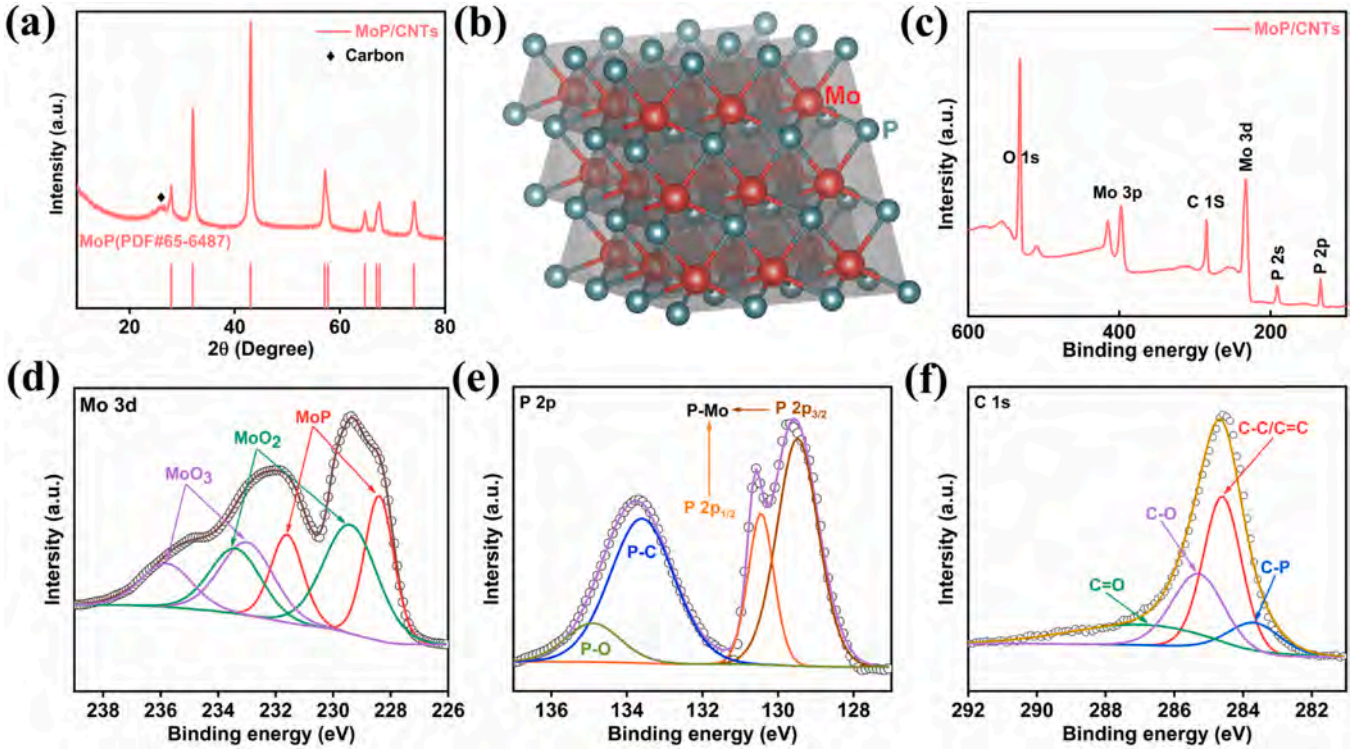

Fig. 3. (a) XRD patterns of MoP/CNTs. (b) Crystal structure of MoP. (c) Survey XPS spectra of MoP/CNTs microspheres. (d–f) The corresponding XPS fitted spectrum of Mo 3d, P 2p and C 1s.

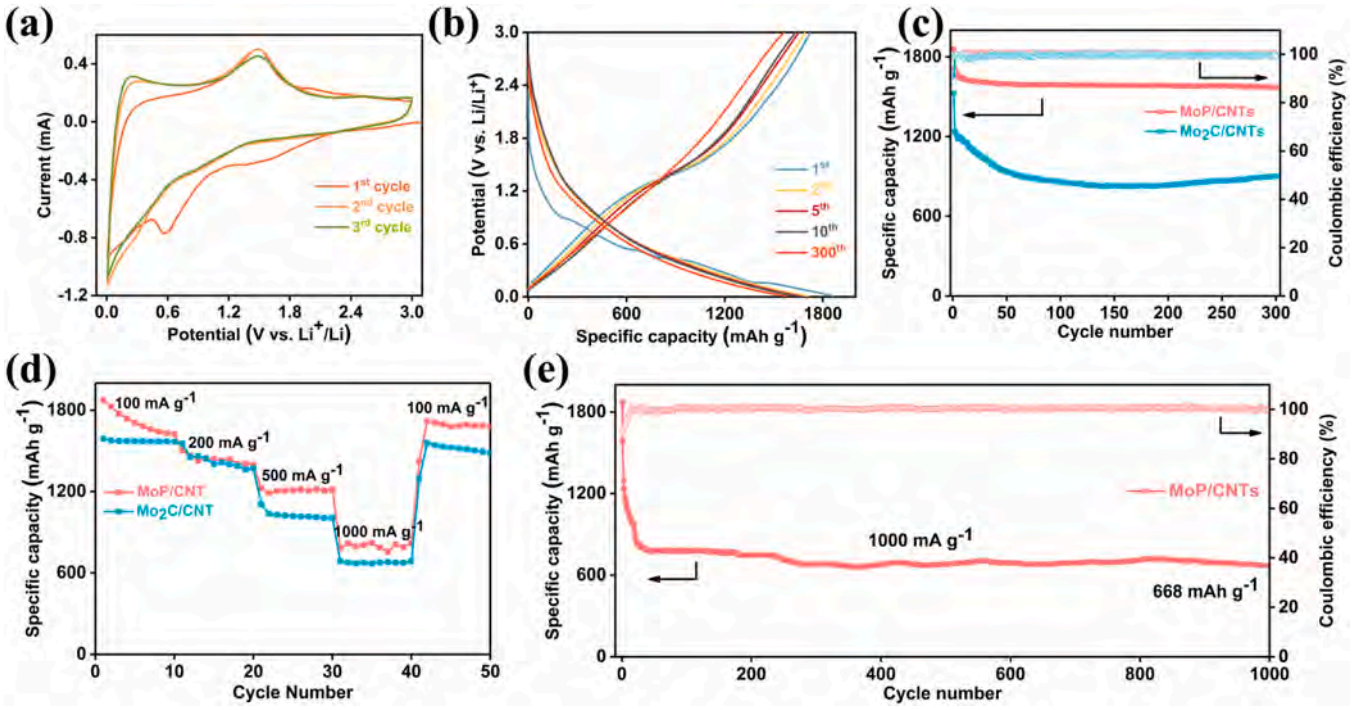

Fig. 4. (a) CV curves of the MoP/CNTs electrode at a scan rate of 0.1 mV s^{-1} in 0.01–3.0 V vs. Li^+/Li. (b) Charge-discharge profiles of the MoP/CNTs anode at 200 mA g^{-1}. (c) Cycling capability of the MoP/CNTs and Mo_2C/CNTs electrodes at a current density of 200 mA g^{-1}. (d) Rate capability of the MoP/CNTs and Mo_2C/CNTs anodes at various current densities. (e) Longer-term cycling performance of the MoP/CNTs electrode at a current density of 1000 mA g^{-1}.

electrode acquired at different scan rates from 0.1 to 1.0 mV s^{-1} are shown in Fig. S5. The charge storage behavior of MoP/CNTs is studied according to the relationship between peak current (I_P) and scan rate (ν) as following Eqs. (1, 2) [54,55]:

$$I_P = a\nu^b \quad (1)$$

or deformation:

$$\log I_p = \log a + b\log\nu \quad (2)$$

Where a and b are adjustable parameters. The b-value represents the dominated charge-storage behavior which exists two conditions: b = 0.5 and b = 1.0. When b-value is 0.5, it is a diffusion-controlled reaction but when b is 1.0, it is a capacitive controlled behavior. By fitting the log ν-log I_P curves (Fig. 5a), the b-value of anodic and cathodic peaks are 0.87 and 0.85, respectively. Hence, the charge storage of MoP/CNTs electrode is mainly controlled by the pseudocapacitive behavior. To analyze quantitatively the capacitive and diffusion contributions in MoP/CNTs electrode, the result is calculated according to the following Eqs. (3, 4) [56]:

$$i = k_1\nu + k_2\nu^{1/2} \quad (3)$$

or deformation:

$$i/\nu^{1/2} = k_1\nu^{1/2} + k_2 \quad (4)$$

The current (i) at a fixed potential (V) contains pseudocapacitive behavior ($k_1\nu$) and diffusion-controlled contributions ($k_2\nu^{1/2}$). k_1 and k_2 can be determined by fitting $i/\nu^{1/2}$ versus $\nu^{1/2}$ to get the slope (k_1) and intercept (k_2), respectively. The current arising from diffusion-controlled and pseudocapacitive processes are able to be distinguished quantitatively. We can see clearly that the surface capacitive mechanism become pronounced at higher sweep rates from Fig. S6 and the pseudocapacitive contribution at 0.5 mV s^{-1} shows a large value (86.6%) (Fig. 5b). The depressed diffusion and dominant capacitive contribution at higher rates are clearly illustrated in Fig. 5c. The results suggest that structural engineering of metal phosphides and CNTs is promising in improving the electrochemical performance of LIBs.

Electrochemical impedance (EIS) spectra is performed to study the charge transfer kinetics of the Mo_2C/CNTs and MoP/CNTs electrodes. Nyquist plots and corresponding equivalent circuit model of Mo_2C/CNTs and MoP/CNTs are shown in Fig. 5d and S7. The R_s and R_f stem from the high frequency region of Z′ axis, which correspond to the impedance of the electrolytes and SEI film, respectively. The charge transfer impedance (R_{ct}) stems from the middle frequency semicircle of the Z′ axis [57]. The MoP/CNTs electrode reveals a smaller value of R_{ct} (48.2 Ω) than that of Mo_2C/CNTs electrode (115.7 Ω) (Table S2). Meanwhile, MoP/CNTs showed a smaller value of R_s (2.3 Ω) than that of Mo_2C/CNTs (8.2 Ω) electrode. Compared with Mo_2C/CNTs electrode, this result further proved that transport of lithium-ions and electrons are easier on the MoP/CNTs electrode.

In order to study the lithium-ion diffusion at the electrode/electrolyte interface, the diffusion coefficients of the lithium ion (D_{Li}) are determined according to Eqs. (5–7) [58,59]:

$$\omega = 2\pi f \quad (5)$$

$$Z' = R_s + R_{ct} + \sigma\omega^{-1/2} \quad (6)$$

$$D_{Li} = \frac{R^2T^2}{2A^2n^4F^4C^2\sigma^2} \quad (7)$$

R is the gas constant (8.314 J mol^{-1} K^{-1}), σ represents the Warburg coefficient, T is Kelvin temperature (298.15 K), A refers to the area of electrodes (2.01 cm^2), n is the electron number, F represents faraday constant (96485 C mol^{-1}) and C refers to the molar concentration of lithium-ion (1 mol L^{-1}). The values of σ can be determined by fitting Z′ versus $\omega^{-1/2}$ and the corresponding values of D_{Li} are calculated from Eq. (7). Fig. 5e demonstrates the fitting result of σ in which there is an apparent smaller slope of MoP/CNTs (68.03 Ω $s^{-1/2}$) compared to Mo_2C/CNTs (91.79 Ω $s^{-1/2}$). Accordingly, the MoP/CNTs has a Li^+ diffusion coefficient of 2.4×10^{-12} cm^2 s^{-1}, which is larger than that of Mo_2C/CNTs (2.6×10^{-13} cm^2 s^{-1}), which suggesting a faster reaction kinetics (from MoP to Li_3P) (Fig. 5f) [28]. The larger

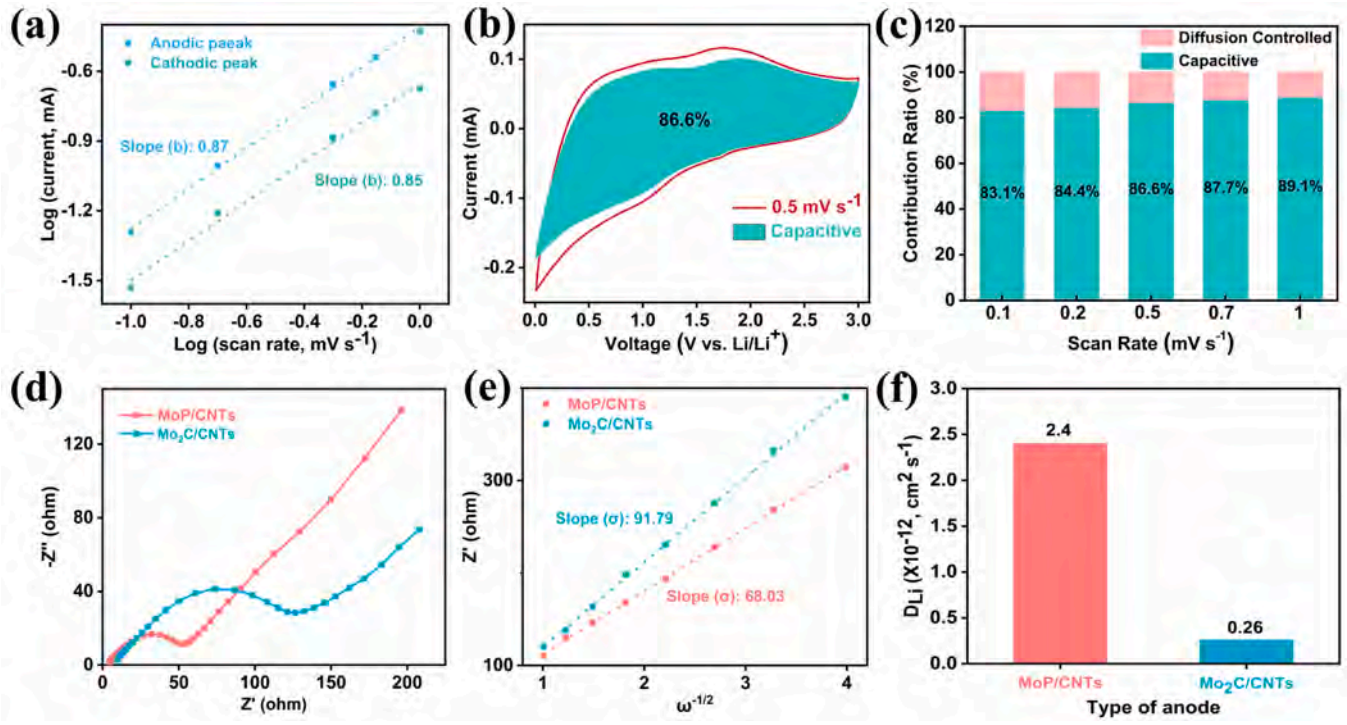

Fig. 5. (a) b value obtained by the slope of plots log ν vs. log I_P for reduction and oxidation states. (b) Capacitive-controlled contribution to the total current at a scan rate of 0.5 mV s^{-1}. (c) Current contribution ratio of capacitive and diffusion-controlled process at different scan rates. (d) Nyquist plots of the MoP/CNTs and Mo_2C/CNTs electrodes. (e) Liner relation of $\omega^{-1/2}$ vs. Z′. (f) D_{Li} of the MoP/CNTs and Mo_2C/CNTs electrodes.

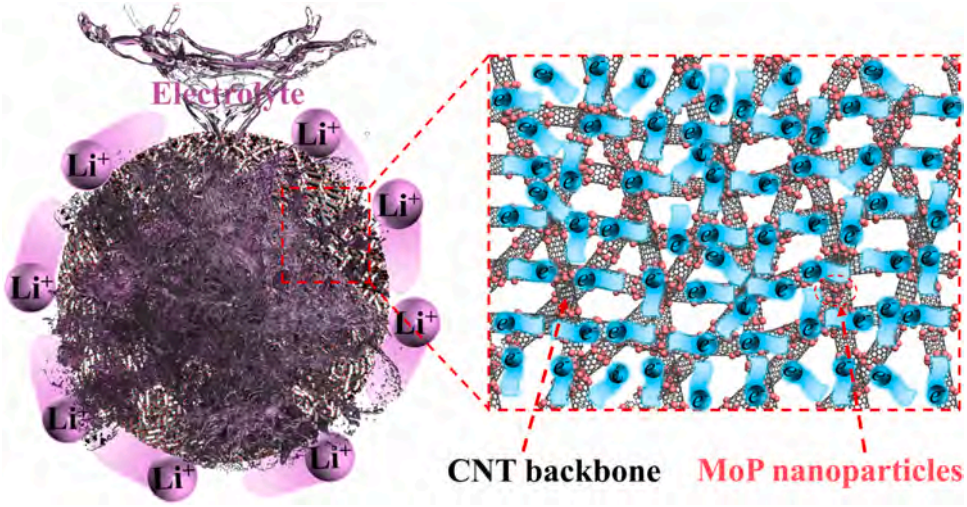

Fig. 6. Schematic illustration for the lithium storage mechanism of the MoP/CNTs electrode.

diffusion coefficient probably comes from the 3D CNTs skeleton and high specific surface area of MoP/CNTs. The lithium storage mechanism of the MoP/CNTs is shown in Fig. 6, and its good lithium storage performance is mainly due to the appropriate combination of the 3D CNTs skeleton and MoP nanoparticles. Therefore, the excellent electrochemical characteristics of MoP/CNTs can be attributed to three factors: 1) The larger specific surface area provides more reaction sites for redox reaction kinetics; 2) The theoretical specific capacity of MoP is high; 3) The synergistic effect of the inlaid structure and the microsphere structure can prevent the collapse of the active material structure during the cycle process, thus improving the long cycle performance of Lithium-ion batteries.

3. Conclusions

In this work, we came up with a two-step strategy combining carbonization and phosphorization to prepare MoP/CNTs as efficient anode materials for LIBs. The 3D CNTs skeleton not only improves the electronic conductivity of the material, but also alleviates the volume change during cycling. Moreover, the unique structure alleviates pulverization of the active material and improves the electrochemical performance of the MoP/CNTs electrode. Therefore, the prepared MoP/CNTs electrode behaved pretty cyclic reversibility of 1568 mAh g^{-1} after 300 cycles at 200 mA g^{-1}. This strategy for preparation of MoP/CNTs is safe and facile, which may provide more approaches for preparing Transition metal phosphates as materials

in other energy applications including other types of batteries and water splitting electrodes.

CRediT authorship contribution statement

Yangbo Wang: Conceptualization, Supervision, Figures processing, Writing - review & editing, Writing - original draft. **Deyang Zhang:** Conceptualization, Writing - review & editing, Writing - original draft. **Ya Yang:** Software, Writing - review & editing. **Ying Guo:** Figures processing, Writing - review & editing. **Zuxue Bai:** Writing - review & editing. **Paul K. Chu:** Writing - review & editing. **Yongsong Luo:** Supervision, Project administration, Funding acquisition.

Declaration of Competing Interest

The authors declare that they have no known competing financial interests or personal relationships that could have appeared to influence the work reported in this paper.

Acknowledgements

This work was financially supported by the National Natural Science Foundation of China (No. 61574122 and 61874093) and the Zhongyuan Thousand Talents Plan-Science & Technology Innovation Leading Talents Project (No. 194200510009), Key Scientific Research Projects of Higher Education Institutions in Henan Province (19A430023), and the Nanhu Scholars Program for Young Scholars of XYNU, and City University of Hong Kong Strategic Research Grants (Nos. 7005105 and 7005264). This work was also supported by the Xinyang Normal University Analysis & Testing Center.

Appendix A. Supporting information

Supplementary data associated with this article can be found in the online version at doi:10.1016/j.jallcom.2021.159608.

References

[1] S.-K. Jung, I. Hwang, D. Chang, K.-Y. Park, S.J. Kim, W.M. Seong, D. Eum, J. Park, B. Kim, J. Kim, J.H. Heo, K. Kang, Nanoscale phenomena in lithium-ion batteries, Chem. Rev. 120 (2020) 6684–6737, https://doi.org/10.1021/acs.chemrev.9b00405

[2] K.P. Lakshmi, R. Deivanayagam, M.M. Shaijumon, Carbon nanotube 'wired' octahedral Sb_2O_3/graphene aerogel as efficient anode material for sodium and lithium ion batteries, J. Alloy. Compd. 857 (2021) 158267, https://doi.org/10.1016/j.jallcom.2020.158267

[3] M. Wang, X. Zhang, X. He, B. Zhu, H. Tang, C. Wang, In-situ grown flower-like C@SnO_2/Cu_2O nanosheet clusters on Cu foam as high performance anode for lithium-ion batteries, J. Alloy. Compd. 856 (2021) 158202, https://doi.org/10.1016/j.jallcom.2020.158202

[4] W.U. YongJian, T. RenHeng, L.I. WenChao, W. Ying, H. Ling, O. LiuZhang, A high-quality aqueous graphene conductive slurry applied in anode of lithium-ion batteries, J. Alloy. Compd. 830 (2020) 154575, https://doi.org/10.1016/j.jallcom.2020.154575

[5] J.-c Zheng, Y.-y Yao, G.-q Mao, H.-z Chen, H. Li, L. Cao, X. Ou, W.-j Yu, Z.-y Ding, H. Tong, Iron-zinc sulfide $Fe_2Zn_3S_5$/$Fe_{1-x}S$@C derived from a metal-organic framework as a high performance anode material for lithium-ion batteries, J. Mater. Chem. A 7 (2019) 16479–16487, https://doi.org/10.1039/C9TA03271A

[6] H. Zhang, A. Hao, Z. Sun, X. Ning, J. Guo, Y. Lv, D. Jia, Boosting the performance of half/full lithium-ion batteries by designing smart architecture anode of SnS_2 nanosheet coating on $NiCo_2S_4$ hollow spheres, J. Alloy. Compd. 847 (2020) 156505, https://doi.org/10.1016/j.jallcom.2020.156505

[7] T. Liu, Y. Zhang, Z. Jiang, X. Zeng, J. Ji, Z. Li, X. Gao, M. Sun, Z. Lin, M. Ling, J. Zheng, C. Liang, Exploring competitive features of stationary sodium ion batteries for electrochemical energy storage, Energy Environ. Sci. 12 (2019) 1512–1533, https://doi.org/10.1039/C8EE03727B

[8] C. An, Y. Yuan, B. Zhang, L. Tang, B. Xiao, Z. He, J. Zheng, J. Lu, Graphene wrapped $FeSe_2$ nano-microspheres with high pseudocapacitive contribution for enhanced Na-ion storage, Adv. Energy Mater. 9 (2019) 1900356, https://doi.org/10.1002/aenm.201900356

[9] Y. Fu, Q. Wei, G. Zhang, S. Sun, Advanced phosphorus-based materials for lithium/sodium-ion batteries: recent developments and future perspectives, Adv. Energy Mater. 8 (2018) 1703058, https://doi.org/10.1002/aenm.201702849

[10] X. Jiao, Y. Liu, B. Li, W. Zhang, C. He, C. Zhang, Z. Yu, T. Gao, J. Song, Amorphous phosphorus-carbon nanotube hybrid anode with ultralong cycle life and high-rate capability for lithium-ion batteries, Carbon 148 (2019) 518–524, https://doi.org/10.1016/j.carbon.2019.03.053

[11] X. Xu, J. Liu, Z. Liu, Z. Wang, R. Hu, J. Liu, L. Ouyang, M. Zhu, FeP@C nanotube arrays grown on carbon fabric as a low potential and freestanding anode for high-performance Li-ion batteries, Small 14 (2018) 1800793, https://doi.org/10.1002/smll.201800793

[12] F. Han, C. Zhang, J. Yang, G. Ma, K. He, X. Li, Well-dispersed and porous FeP@C nanoplates with stable and ultrafast lithium storage performance through conversion reaction mechanism, J. Mater. Chem. A 4 (2016) 12781–12789, https://doi.org/10.1039/C6TA04521A

[13] C. Lin, R. Hu, J. Liu, L. Yang, J. Liu, L. Ouyang, M. Zhu, A nanorod FeP@phosphorus-doped carbon composite for high-performance lithium-ion batteries, J. Alloy. Compd. 763 (2018) 296–304, https://doi.org/10.1016/j.jallcom.2018.05.219

[14] P.K. Nayak, L. Yang, W. Brehm, P. Adelhelm, From lithium-ion to sodium-ion batteries: advantages, challenges, and surprises, Angew. Chem. Int. Ed. 57 (2018) 102–120, https://doi.org/10.1002/anie.201703772

[15] J. Ni, X. Bi, Y. Jiang, L. Li, J. Lu, Bismuth chalcogenide compounds Bi_2X_3 (X=O, S, Se): applications in electrochemical energy storage, Nano Energy 34 (2017) 356–366, https://doi.org/10.1016/j.nanoen.2017.02.041

[16] Z. Liu, S. Yang, B. Sun, X. Chang, J. Zheng, X. Li, A peapod-like CoP@C nanostructure from phosphorization in a low-temperature molten salt for high-performance lithium-ion batteries, Angew. Chem. Int. Ed. 57 (2018) 10187–10191, https://doi.org/10.1002/anie.201805468

[17] R. Wang, X.-Y. Dong, J. Du, J.-Y. Zhao, S.-Q. Zang, MoF-derived bifunctional Cu_3P nanoparticles coated by a N,P-codoped carbon shell for hydrogen evolution and oxygen reduction, Adv. Mater. 30 (2018) 1703711, https://doi.org/10.1002/adma.201703711

[18] P. Lou, Z. Cui, Z. Jia, J. Sun, Y. Tan, X. Guo, Monodispersed carbon-coated cubic NiP_2 nanoparticles anchored on carbon nanotubes as ultra-long-life anodes for reversible lithium storage, ACS Nano 11 (2017) 3705–3715, https://doi.org/10.1021/acsnano.6b08223

[19] C. Ma, C. Deng, X. Liao, Y. He, Z. Ma, H. Xiong, Urchin-like MoP nanocrystals embedded in N-doped carbon as high rate lithium ion battery anode, ACS Appl. Energy Mater. 1 (2018) 7140–7145, https://doi.org/10.1021/acsaem.8b01580

[20] X. Fan, T. Gao, C. Luo, F. Wang, J. Hu, C. Wang, Superior reversible tin phosphide-carbon spheres for sodium ion battery anode, Nano Energy 38 (2017) 350–357, https://doi.org/10.1016/j.nanoen.2017. 06.014

[21] Y. Zhang, H. Zhang, Y. Feng, L. Liu, Y. Wang, Unique Fe_2P nanoparticles enveloped in sandwich like graphited carbon sheets as excellent hydrogen evolution reaction catalyst and lithium-ion battery anode, ACS Appl. Mater. Interfaces 7 (2015) 26684–26690, https://doi.org/10.1021/acsami.5b08620

[22] Y. Yang, M. Luo, Y. Xing, S. Wang, W. Zhang, F. Lv, Y. Li, Y. Zhang, W. Wang, S. Guo, A universal strategy for intimately coupled carbon nanosheets/MoM nanocrystals (M = P, S, C, and O) hierarchical hollow nanospheres for hydrogen evolution catalysis and sodium-ion storage, Adv. Mater. 30 (2018) 1706085, https://doi.org/10.1002/adma.201706085

[23] Y. Mi, W. Liu, X. Li, J. Zhuang, H. Zhou, H. Wang, High-performance Li-S battery cathode with catalyst-like carbon nanotube-MoP promoting polysulfide redox, Nano Res. 10 (2017) 3698–3705, https://doi.org/10.1007/s12274-017-1581-8

[24] Y. Yin, L. Fan, Y. Zhang, N. Liu, N. Zhang, K. Sun, MoP hollow nanospheres encapsulated in 3D reduced graphene oxide networks as high rate and ultralong cycle performance anodes for sodium-ion batteries, Nanoscale 11 (2019) 7129–7134, https://doi.org/10.1039/C9NR00406H

[25] S. Wang, W. Ma, X. Zang, L. Ma, L. Tang, J. Guo, Q. Liu, X. Zhang, VS_4-decorated carbon nanotubes for lithium storage with pseudocapacitance contribution, ChemSusChem 13 (2020) 1637–1644, https://doi.org/10.1002/cssc.201901412

[26] M.G. Kim, S. Lee, J. Cho, Highly reversible Li-ion intercalating MoP nanoparticle cluster anode for lithium rechargeable batteries, J. Electrochem. Soc. 156 (2009) A89, https://doi.org/10.1149/1.3032115

[27] X. Yang, Q. Li, H. Wang, J. Feng, M. Zhang, R. Yuan, Y. Chai, Preparation of porous MoP-C microspheres without a hydrothermal process as a high capacity anode for lithium ion batteries, Inorg. Chem. Front. 5 (2018) 1432–1437, https://doi.org/10.1039/C8QI00243F

[28] C. Fu, H. Yang, G. Feng, L. Wang, T. Liu, In-situ reducing synthesis of MoP@nitrogen-doped carbon nanofibers as an anode material for lithium/sodium-ion batteries, Electrochim. Acta 358 (2020) 136921, https://doi.org/10.1016/j.electacta.2020.136921

[29] D. Yang, J. Zhu, X. Rui, H. Tan, R. Cai, H.E. Hoster, D.Y.W. Yu, H.H. Hng, Q. Yan, Synthesis of cobalt phosphides and their application as anodes for lithium ion batteries, ACS Appl. Mater. Interfaces 5 (2013) 1093–1099, https://doi.org/10.1021/am302877q

[30] D. Kong, X. Li, Y. Zhang, X. Hai, W. Bin, X. Qiu, Q. Song, Q.-H. Yang, L. Zhi, Correction: encapsulating V_2O_5 into carbon nanotubes enables the synthesis of flexible high-performance lithium ion batteries, Energy Environ. Sci. 9 (2016) 2666, https://doi.org/10.1039/C6EE90043G

[31] G.D. Park, J.H. Choi, D.S. Jung, J.-S. Park, Y.C. Kang, Three-dimensional porous pitch-derived carbon coated Si nanoparticles-CNT composite microsphere with superior electrochemical performance for lithium ion batteries, J. Alloy. Compd. 821 (2020) 153224, https://doi.org/10.1016/j.jallcom.2019 153224.

[32] W. Luo, X. Chen, Y. Xia, M. Chen, L. Wang, Q. Wang, W. Li, J. Yang, Surface and interface engineering of silicon-based anode materials for lithium-ion batteries, Adv. Energy Mater. 7 (2017) 1701083, https://doi.org/10.1002/aenm.201701083

[33] Z. Sun, X.-L. Wu, Z. Peng, J. Wang, S. Gan, Y. Zhang, D. Han, L. Niu, Lithium-sulfur batteries: compactly coupled nitrogen-doped carbon nanosheets/molybdenum phosphide nanocrystal hollow nanospheres as polysulfide reservoirs for high-performance lithium-sulfur chemistry, Small 15 (2019) 1970216, https://doi.org/10.1002/smll.201970216
[34] C. Pi, C. Huang, Y. Yang, H. Song, X. Zhang, Y. Zheng, B. Gao, J. Fu, P.K. Chu, K. Huo, In situ formation of N-doped carbon-coated porous MoP nanowires: a highly efficient electrocatalyst for hydrogen evolution reaction in a wide PH range, Appl. Catal. B: Environ. 263 (2020) 118358, https://doi.org/10.1016/j.apcatb.2019.118358
[35] J. Tian, Q. Liu, A.M. Asiri, X. Sun, Self-supported nanoporous cobalt phosphide nanowire arrays: an efficient 3D hydrogen-evolving cathode over the wide range of PH 0-14, J. Am. Chem. Soc. 136 (2014) 7587–7590, https://doi.org/10.1021/ja503372r
[36] A. Jiang, Z. Wang, Q. Li, M. Dong, Ionic liquid-assisted synthesis of hierarchical one-dimensional MoP/NPC for high-performance supercapacitor and electrocatalysis, ACS Sustain. Chem. Eng. 8 (2020) 6343–6351, https://doi.org/10.1021/acssuschemeng.0c00238
[37] M. Pramanik, S. Tominaka, Z.-L. Wang, T. Takei, Y. Yamauchi, Mesoporous semimetallic conductors: structural and electronic properties of cobalt phosphide systems, Angew. Chem. Int. Ed. 56 (2017) 13508–13512, https://doi.org/10.1002/anie.201707878
[38] X. Wang, P. Sun, J. Qin, J. Wang, Y. Xiao, M. Cao, A three-dimensional porous MoP@C hybrid as a high-capacity, long-cycle life anode material for lithium-ion batteries, Nanoscale 8 (2016) 10330–10338, https://doi.org/10.1039/C6NR01774F
[39] D. Wang, Y. Shen, X. Zhang, Z. Wu, Enhanced hydrogen evolution from the MoP/C hybrid by the modification of Ketjen Black, J. Mater. Sci. 52 (2017) 3337–3343, https://doi.org/10.1007/s10853-01 6-0621-1
[40] X. Zhang, X. Yu, L. Zhang, F. Zhou, Y. Liang, R. Wang, Molybdenum phosphide/carbon nanotube hybrids as PH-universal electrocatalysts for hydrogen evolution reaction, Adv. Funct. Mater. 28 (2018) 1706523, https://doi.org/10.1002/adfm.201706523
[41] Y. Lu, J.-P. Tu, Q.-Q. Xiong, J.-Y. Xiang, Y.-J. Mai, J. Zhang, Y.-Q. Qiao, X.-L. Wang, C.-D. Gu, S.X. Mao, Controllable synthesis of a monophase nickel phosphide/carbon (Ni_5P_4/C) composite electrode via wet-chemistry and a solid-state reaction for the anode in lithium secondary batteries, Adv. Funct. Mater. 22 (2012) 3927–3935, https://doi.org/10.1002/adfm.201102660
[42] S. Liu, H. Xu, X. Bian, J. Feng, J. Liu, Y. Yang, C. Yuan, Y. An, R. Fan, L. Ci, Nanoporous red phosphorus on reduced graphene oxide as superior anode for sodium-ion batteries, ACS Nano 12 (2018) 7380–7387, https://doi.org/10.1021/acsnano.8b04075
[43] N. Chen, Q. Mo, L. He, X. Huang, L. Yang, J. Zeng, Q. Gao, Heterostructured MoC-MoP/N-doped carbon nanofibers as efficient electrocatalysts for hydrogen evolution reaction, Electrochim. Acta 299 (2019) 708–716, https://doi.org/10.1016/j.electacta.2019.01.054
[44] J. Zhang, R. Sui, Y. Xue, X. Wang, J. Pei, X. Liang, Z. Zhuang, Direct synthesis of parallel doped N-MoP/N-CNT as highly active hydrogen evolution reaction catalyst, Sci. China Mater. 62 (2019) 690–698, https://doi.org/10.1007/s40843-018-9360-1
[45] H. Yu, S. Cao, B. Fu, Z. Wu, J. Liu, L. Piao, Self-supported nanotubular MoP electrode for highly efficient hydrogen evolution via water splitting, Catal. Commun. 127 (2019) 1–4, https://doi.org/10.1016/j.catcom.2019.04.018
[46] G. Li, Y. Sun, J. Rao, J. Wu, A. Kumar, Q.N. Xu, C. Fu, E. Liu, G.R. Blake, P. Werner, B. Shao, K. Liu, S. Parkin, X. Liu, M. Fahlman, S.-C. Liou, G. Auffermann, J. Zhang, C. Felser, X. Feng, Carbon-tailored semimetal MoP as an efficient hydrogen evolution electrocatalyst in both alkaline and acid media, Adv. Energy Mater. 8 (2018) 1801258, https://doi.org/10.1002/aenm.201801258
[47] W. Cui, Q. Liu, Z. Xing, A.M. Asiri, K.A. Alamry, X. Sun, MoP nanosheets supported on biomass-derived carbon flake: one-step facile preparation and application as a novel high-active electrocatalyst toward hydrogen evolution reaction, Appl. Catal. B 164 (2015) 144–150, https://doi.org/10.1016/j.apcatb.2014.09.016
[48] X. Wang, J. Feng, Y. Bai, Q. Zhang, Y. Yin, Synthesis, properties, and applications of hollow micro-/nanostructures, Chem. Rev. 116 (2016) 10983–11060, https://doi.org/10.1021/acs.chemrev.5b00731
[49] J.W. Hall, N. Membreno, J. Wu, H. Celio, R.A. Jones, K.J. Stevenson, Low-temperature synthesis of amorphous FeP_2 and its use as anodes for Li ion batteries, J. Am. Chem. Soc. 134 (2012) 5532–5535, https://doi.org/10.1021/ja301173q
[50] Y. Shi, B. Guo, S.A. Corr, Q. Shi, Y.-S. Hu, K.R. Heier, L. Chen, R. Seshadri, G.D. Stucky, Ordered mesoporous metallic MoO_2 materials with highly reversible lithium storage capacity, Nano Lett. 9 (2009) 4215–4220, https://doi.org/10.1021/nl902423a
[51] Z. Wu, W. Lei, J. Wang, R. Liu, K. Xia, C. Xuan, D. Wang, Various structured molybdenum-based nanomaterials as advanced anode materials for lithium ion batteries, ACS Appl. Mater. Interfaces 9 (2017) 12366–12372, https://doi.org/10.1021/acsami.6b16251
[52] H. Kim, W. Choi, J. Yoon, J. Um, W. Lee, K. Jaeyoung, J. Cabana, W.-S. Yoon, Exploring anomalous charge storage in anode materials for next-generation Li rechargeable batteries, Chem. Rev. 120 (2020) 6934–6976, https://doi.org/10.1021/acs.chemrev.9b00618
[53] Y. Ma, U. Ulissi, D. Bresser, Y. Ma, Y. Ji, S. Passerini, Manganese silicate hollow spheres enclosed in reduced graphene oxide as anode for lithium-ion batteries, Electrochim. Acta 258 (2017) 535–543, https://doi.org/10.1016/j.electacta.2017.11.096
[54] V. Augustyn, J. Come, M.A. Lowe, J.W. Kim, P.-L. Taberna, S.H. Tolbert, H.D. Abruña, P. Simon, B. Dunn, High-rate electrochemical energy storage through Li^+ intercalation pseudocapacitance, Nat. Mater. 12 (2013) 518–522, https://doi.org/10.1038/nmat3601
[55] L. Wang, G. Yang, J. Wang, S. Wang, C. Wang, S. Peng, W. Yan, S. Ramakrishna, In situ fabrication of branched TiO_2/C nanofibers as binder-free and free-standing anodes for high-performance sodium-ion batteries, Small 15 (2019) 1901584, https://doi.org/10.1002/smll.201901584
[56] X. Hui, R. Zhao, P. Zhang, C. Li, C. Wang, L. Yin, Low-temperature reduction strategy synthesized Si/Ti_3C_2 MXene composite anodes for high-performance Li-ion batteries, Adv. Energy Mater. 9 (2019) 1901065, https://doi.org/10.1002/aenm.201901065
[57] X. Miao, R. Yin, X. Ge, Z. Li, L. Yin, Ni_2P@carbon core-shell nanoparticle-arched 3D interconnected graphene aerogel architectures as anodes for high-performance sodium-ion batteries, Small 13 (2017) 1702138, https://doi.org/10.1002/smll.201702138
[58] X. Yang, A. Rogach, Electrochemical techniques in battery research: a tutorial for nonelectrochemists, Adv. Energy Mater. 9 (2019) 1900747, https://doi.org/10.1002/aenm.201900747
[59] H. Zhang, P. Zong, M. Chen, H. Jin, Y. Bai, S. Li, F. Ma, H. Xu, K. Lian, In situ synthesis of multilayer carbon matrix decorated with copper particles: enhancing the performance of Si as anode for Li-ion batteries, ACS Nano 13 (2019) 3054–3062, https://doi.org/10.1021/acsnano.8b08088

Supporting Information

Three-Dimensional Nano/Micro-Structured Porous MoP/CNTs Microspheres as High-Capacity Anode for Lithium-Ion Batteries

Yangbo Wang,[a,1] Deyang Zhang,[a,c,1,*] Ya Yang,[a] Ying Guo,[a] Zuxue Bai,[a] Paul K. Chu[c] and Yongsong Luo[a,b,*]

[a] Key Laboratory of Microelectronics and Energy of Henan Province, Henan Joint International Research Laboratory of New Energy Storage Technology, Xinyang Normal University, Xinyang d6d000, P. R. China.

[b] College of Physics and Electronic Engineering, Nanyang Normal University, Nanyang 473061, China.

[c] Department of Physics, Department of Materials Science & Engineering, and Department of Biomedical Engineering, City University of Hong Kong, Tat Chee Avenue, Kowloon, Hong Kong, China.

[*] Corresponding author. Tel./fax: +86 376 6391760, E-mail: ysluo@xynu.edu.cn (Y. S. Luo), zdy@xynu.edu.cn (D. Y. Zhang).

[1] These authors contributed equally to this work.

Experimental section

Synthesis of Mo_2C/CNTs microspheres

In brief, 0.05 g of acid treated functionalized CNTs [1] (prepared by modified Hummers method) were added to a mixture solution containing 20 mL of DI water and 40 mL of ethanol, then which was dispersed by ultrasonication for 40 min. Afterwards, 0.15 g of ammonium molybdate tetrahydrate and 0.25 g of sucrose were added successively to the dispersed CNT solution. After stirring for two hours, the above solution was spray-dried at 180 °C in air with a feed rate of 600 ml h^{-1}. The powders obtained were heated to 800 °C from the room temperature with a ramping rate of 2 °C min^{-1} and then annealed at 800 °C for 5 h in Ar atmosphere to obtain the Mo_2C/CNTs microspheres.

Synthesis of MoP/CNTs microspheres

In the synthesis of MoP/CNTs, the Mo_2C/CNTs and NaH_2PO_2 were placed on two different crucibles with a mass ratio of 1: 26 and placed in the upstream and middle part of the furnace, respectively. Subsequently, the furnace was heated to 800 °C at a rate of 5 °C min^{-1} and held for 2 h in a static argon atmosphere [2]. The sample was retrieved from the crucible in the middle of the furnace after cooling, which is the final product MoP/CNTs microspheres.

Material Characterization

The morphology of materials was examined by the scanning electron microscope (SEM, Hitachi S-4800, Japan) and the phase was determined by powder X-ray diffraction (XRD, Bruker D2 PHASER, Germany). Transmission electron microscopy was carried out by a FETEM (TEM, Tecnai G2 F20, USA) to analyze the microstructures. Elemental composition and atomic bonding information were obtained by X-ray Photoelectron Spectroscopy (XPS, K-ALPHA 0.5 eV, USA). The obtained adsorption-desorption isotherms (BET, ASAP 2460, USA) were evaluated to determine the pore parameters including specific surface area and pore size. Thermogravimetric analysis (TGA) measurements were performed on aSTA499f5 analyzer.

Electrochemical Measurements

The electrodes for lithium ion batteries (LIBs) were prepared by mixing the electro-active material, conductive carbon material and polymer binder with a weight ratio of 7: 2: 1 to form a homogeneous suspension. The area of each electrode is ~2 cm^2 and the areal density of active material for each electrode is ~1.2 mg cm^{-2}. The batteries were assembled in glove box (Lab-

2000, China) under Ar atmosphere with Li-metal foil as the counter electrode, celgard (2500) as the separator, and 1 M $LiPF_6$ solution containing diethyl carbon as well as ethylene carbonate (1: 1, volume) as the electrolyte. Galvanostatic cycling was conducted with CR2032 cells on the battery-testing system (Neware CT-3008, China) in the voltage range between 0.01 and 3.0 V. Cyclic voltammetry (CV) was carried out on a VMP3 electrochemical workstation under different scanning rates. Electrochemical impedance spectroscopy (EIS) was performed by applying a sine wave with an amplitude of 0.5 mV in the frequency range of 10 mHz-100 kHz. Charge/discharge tests were done using a Neware battery testing system in the potential range from 0.01 to 3.0 V (vs. Li^+/Li).

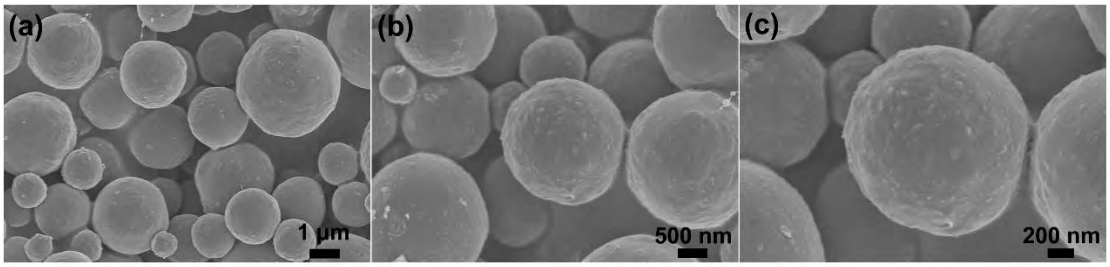

Fig. S1. SEM image of Mo_2C/CNTs.

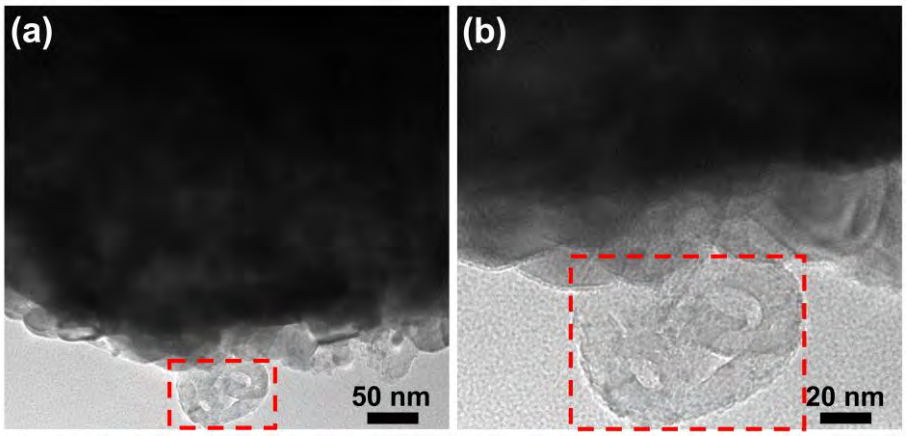

Fig. S2. TEM images of MOP/CNT microspheres.

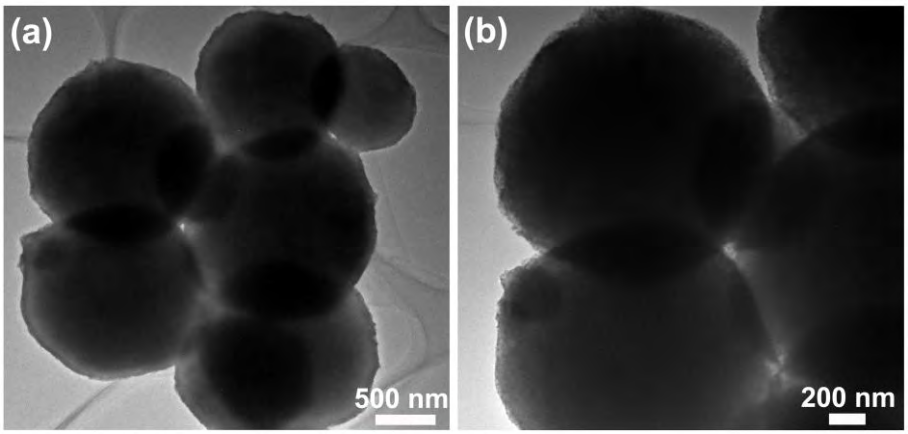

Fig. S3. TEM images of Mo_2C/CNTs.

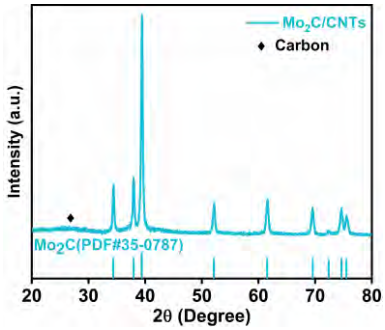

Fig. S4. XRD pattern of the Mo_2C@CNTs.

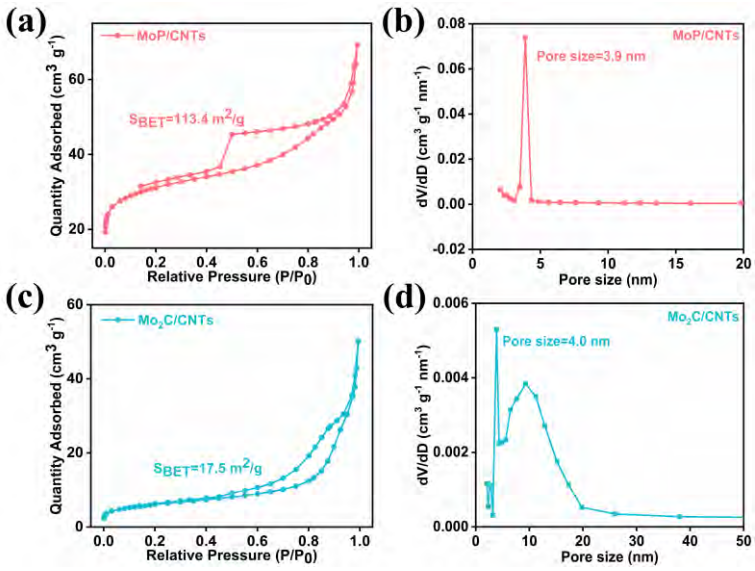

Fig. S5. (a) BET curve of the MoP/CNTs. (b) Pore size distribution curve of the MoP/CNTs. (c) BET curve of the Mo_2C/CNTs. (d) Pore size distribution curve of the Mo_2C/CNTs.

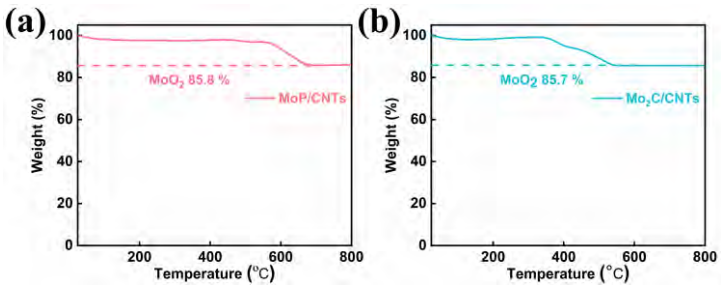

Fig. S6. Thermal gravimetric (TGA) profiles of the Mo_2C/CNTs and MoP/CNTs in air with a heating rate of 5 °C min^{-1}.

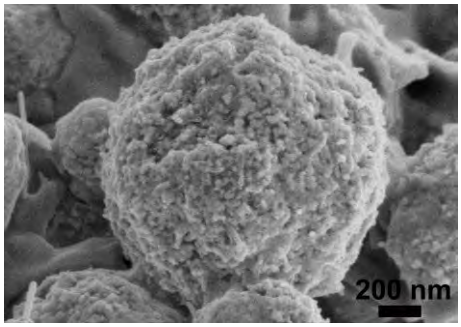

Fig. S7. SEM images of MoP/CNTs after 300 cycles.

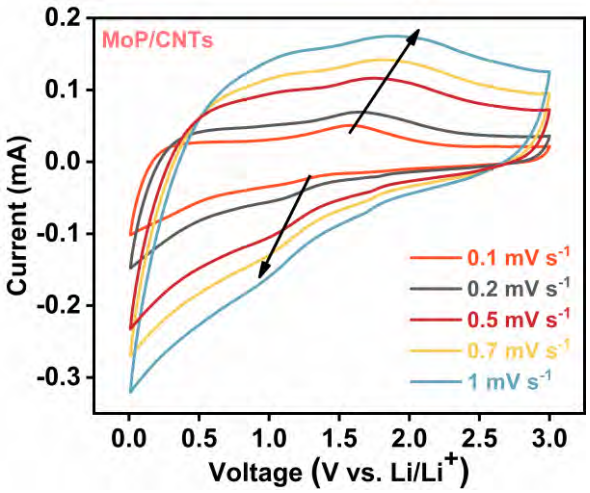

Fig. S7. CV curves of the MoP/CNTs electrode at different scan rates from 0.1 to 1 mV s^{-1}.

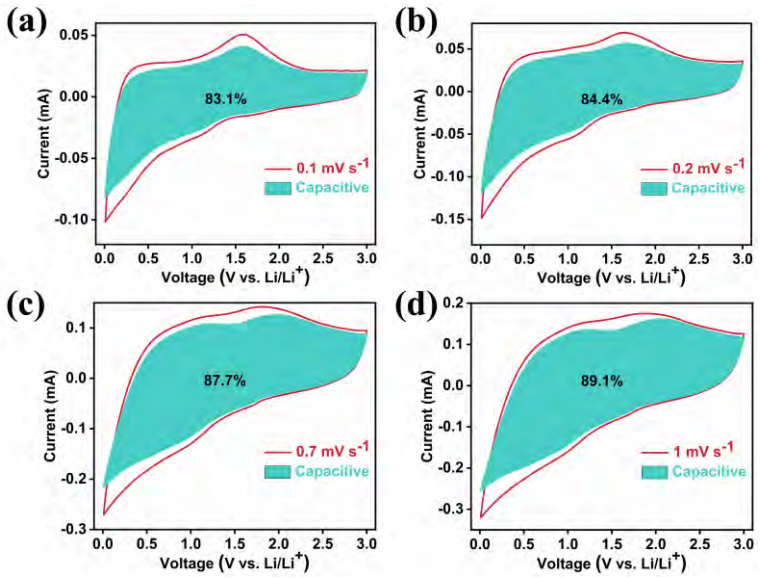

Fig. S8. (a-d) Separation charge contributions of the capacitive and diffusion-controlled proportions at scan rate of 0.1, 0.2, 0.7 and 1 mV s^{-1} for the MoP/CNTs electrode.

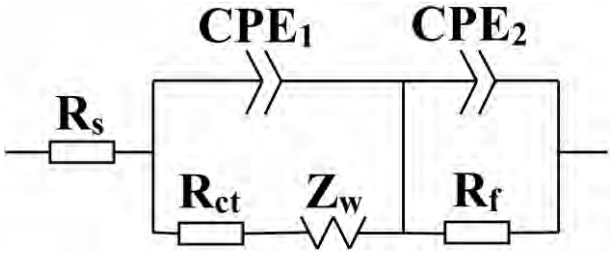

Fig. S9. Equivalent circuit for the EIS experimental data.

Table S1 Comparison of different metal phosphide anodes in the literature and our anode described in this paper.

Anodes	Retention capacity (mAh g^{-1})	Current density (mA g^{-1})	Reference
MoP-C	575 (100^{th} cycle)	100	[3]
MoP@NCNFs	840 (200^{th} cycle)	100	[4]
$Ni_{12}P_5$@C/GNS	900 (100^{th} cycle)	100	[5]
MoP@C	1028 (100^{th} cycle)	100	[6]
Ni_2P/C	324 (200^{th} cycle)	200	[7]
Peapod-like CoP@C	720 (50^{th} cycle)	200	[8]
MoP/CNTs microsphere	660 (1000^{th} cycle)	200	**This work**

Table S2 Fitted electrochemical resistance parameters of the Mo_2C/CNTs and MoP/CNTs electrodes for lithium storage.

Sample	R_s (Ω)	R_f (Ω)	R_{ct} (Ω)
Mo_2C/CNTs	8.2	9.5	115.7
MoP/CNTs	2.3	2.9	48.2

Reference:

[1] Y. Liang, H. Wang, P. Diao, W. Chang, G. Hong, Y. Li, M. Gong, L. Xie, J. Zhou, J. Wang, T.Z. Regier, F. Wei, H. Dai, Oxygen reduction electrocatalyst based on strongly coupled cobalt oxide nanocrystals and carbon nanotubes, J. Am. Chem. Soc. 134 (2012) 15849-15857. http://dx.doi.org/10.1021/ja305623m.

[2] Y. Zhang, Y. Wang, R. Luo, Y. Yang, Y. Lu, Y. Guo, X. Liu, S. Cao, J.K. Kim, Y. Luo, A 3D porous FeP/rGO modulated separator as a dual-function polysulfide barrier for high-performance lithium sulfur batteries, Nanoscale Horiz. 5 (2020) 530-540. http://dx.doi.org/10.1039/c9nh00532c.

[3] Z. Wu, W. Lei, J. Wang, R. Liu, K. Xia, C. Xuan, D. Wang, Various Structured Molybdenum-based Nanomaterials as Advanced Anode Materials for Lithium ion Batteries, ACS Appl. Mater. Interfaces 9 (2017) 12366-12372. http://dx.doi.org/10.1021/acsami.6b16251.

[4] C. Fu, H. Yang, G. Feng, L. Wang, T. Liu, In-situ reducing synthesis of MoP@nitrogen-doped carbon nanofibers as an anode material for lithium/sodium-ion batteries, Electrochim. Acta 358 (2020) 136921. https://doi.org/10.1016/j.electacta.2020.136921.

[5] H. Guo, C. Chen, K. Chen, H. Cai, X. Chang, S. Liu, W. Li, Y. Wang, C. Wang, High performance carbon-coated hollow $Ni_{12}P_5$ nanocrystals decorated on GNS as advanced anodes for lithium and sodium storage, J. Mater. Chem. A. 5 (2017) 22316-22324. http://dx.doi.org/10.1039/C7TA06843C.

[6] X. Wang, P. Sun, J. Qin, J. Wang, Y. Xiao, M. Cao, A three-dimensional porous MoP@C hybrid as a high-capacity, long-cycle life anode material for lithium-ion batteries, Nanoscale 8 (2016) 10330-10338. http://dx.doi.org/10.1039/C6NR01774F.

[7] Y.-S. Kim, M.-C. Kim, S.-H. Moon, H. Kim, K.-W. Park, Ni_2P/graphitic carbon nanostructure electrode with superior electrochemical performance, Electrochim. Acta 341 (2020) 136045. https://doi.org/10.1016/j.electacta.2020.136045.

[8] Z. Liu, S. Yang, B. Sun, X. Chang, J. Zheng, X. Li, A Peapod-like CoP@C Nanostructure from Phosphorization in a Low-Temperature Molten Salt for High-Performance Lithium-Ion Batteries, Angew. Chem. Int. Ed. 57 (2018) 10187-10191. https://doi.org/10.1002/anie.201805468.